Pd-P antibonding interactions in APd$_2$P$_2$ ($A =$ Ca and Sr) superconductors

Joanna Blawat,[1,2] Przemyslaw Wojciech Swatek,[3,4] Debarchan Das ![ORCID],[5] Dariusz Kaczorowski ![ORCID],[5]
Rongying Jin,[1] and Weiwei Xie ![ORCID][2]

[1]*Department of Physics and Astronomy, Louisiana State University, Baton Rouge, Louisiana 70803, USA*
[2]*Department of Chemistry, Louisiana State University, Baton Rouge, Louisiana 70803, USA*
[3]*Division of Materials Science and Engineering, Ames Laboratory, Ames, Iowa 50011, USA*
[4]*Department of Physics and Astronomy, Iowa State University, Ames, Iowa 50011, USA*
[5]*Institute of Low Temperature and Structure Research, Polish Academy of Sciences, P. O. Box 1410, 50-950, Wroclaw, Poland*

We report the observation of superconductivity in single-crystalline CaPd$_2$P$_2$ and SrPd$_2$P$_2$ obtained from Bi-flux. Both CaPd$_2$P$_2$ and SrPd$_2$P$_2$ crystallize in the ThCr$_2$Si$_2$-type structure (space group $I4/mmm$) with a short P-P distance. Electrical resistivity and specific heat measurements conjointly corroborate bulk superconductivity at $T_c \sim 1.0$ K with $\Delta C/\gamma T_c = 1.42$ for CaPd$_2$P$_2$, and $T_c \sim 0.7$ K with $\Delta C/\gamma T_c = 1.47$ for SrPd$_2$P$_2$. The electronic structure calculations and chemical bonding analysis indicate that Pd-P antibonding interactions primarily dominate around the Fermi level and play the critical role in inducing superconductivity.

I. INTRODUCTION

Superconductors are known to carry electricity without any loss. Even after more than a hundred years of its discovery, superconductivity remains unpredictable and puzzling. In the framework of the Bardeen-Cooper-Schrieffer (BCS) theory [1], electron-phonon coupling induces electron-electron pairing (Cooper pair) with the opposite spins and crystal momenta. From a chemistry perspective, Cooper pairs can be approximately considered as a format of "resonance" between the atoms, which host the right kind of charge transfer to induce superconductivity in the system. Clear examples of such critical charge-transfer pairs for superconductivity in the periodic table are Cu-O and Fe-As in two high-T_c superconducting families [2–5]. In addition, Pd- and Pt- contained intermetallic superconductors may exhibit some intriguing structure and physical properties. For example, SrPt$_2$As$_2$ reveals the coexistence of superconductivity and charge density waves [6]. Superconducting SrPt$_6$P$_2$ ($T_c = 0.6$ K) consists of a unique three-dimensional network of vertex shared distorted Pt$_6$P trigonal prisms [7]. UPd$_2$Al$_3$ is a heavy-fermion superconductor with $T_c \sim 2.0$ K and antiferromagnetic transition at $\sim$14.0 K [8].

Our previous work showed Pt-Bi antibonding interactions might play a key role in superconductivity observed in BaPt$_2$Bi$_2$, while Bi-Bi bonds between layers are weak [9]. This is true for many 122-type superconductors. For example, there is negligible P-P bonding between adjacent layers in superconducting BaIr$_2$P$_2$, BaRh$_2$P$_2$, or BaNi$_2$P$_2$ [10,11]. Density of states (DOS) calculations indicate that d orbitals in transition metals dominate around Fermi level, which play the critical role in their physical properties, especially superconductivity [7,12]. We thus choose APd$_2$P$_2$ ($A =$ Ca and Sr) to study the correlation between superconductivity and atomic interactions (P-P and Pd-P).

In this paper, we report the single-crystal growth, electrical transport and thermodynamic measurements probing the superconducting properties and electronic structure calculations of APd$_2$P$_2$ ($A =$ Ca and Sr). We show that APd$_2$P$_2$ ($A =$ Ca and Sr) undergoes superconducting transition with a critical temperature $T_c \sim 1.0$ K for $A =$ Ca and 0.7 K for $A =$ Sr. Specific heat data confirm bulk superconductivity with weak coupling. The theoretical assessments indicate the Pd-P antibonding instead of P-P bonding interactions dominates the Fermi level and presumably strongly associated with the superconductivity.

II. METHODS

The single crystals of CaPd$_2$P$_2$ and SrPd$_2$P$_2$ were grown using the flux method. The elemental Ca granules (99.5%, Alfa Aesar), Sr rod (>99%, Alfa Aesar), Pd powder (99.95%, Alfa Aesar), P lump (99.999%, BCS), and Bi rod (99.99%, Alfa Aesar) with molar ratio of Ca/Sr : Pd : P : Bi = 3 : 4 : 4 : 25 were taken in alumina crucibles and sealed in evacuated quartz tubes. The total mass of used element was $\sim$2 g. The tubes were slowly (60 °C/h) heated up to 600 °C and held at this temperature for 5 hours to avoid an explosion of red phosphorus, and then heated up to 1050 °C. The samples were kept for 5 hours and then cooled rapidly down to 900°C followed by slow cooling (-3 °C/h) to 550 °C. The remaining Bi flux was centrifuged at 550 °C and shiny platelike single crystals with typical dimensions $\sim$2 $\times$ 2 $\times$ 0.2 mm^3 were obtained. The single crystals of CaPd$_2$P$_2$ and SrPd$_2$P$_2$ are stable in the air.

The crystal structures were examined by a Bruker Apex II single x-ray diffractometer equipped with Mo radiation ($\lambda_{K\alpha} = 0.71073$ Å). The SHELXLTL [13] package was used to solve the crystal structure with the full-matrix least-squares method. The samples were further examined by powder x-ray diffraction (PXRD) using Rigaku MiniFlex 600 diffractometer with Cu K$_{\alpha 1}$ radiation ($\lambda = 1.5406$ Å). The PXRD patterns were analyzed by means of the Le Bail method [14]

using the FULLPROF software [15]. The drawings of crystal structure were done using VESTA software [16].

The electrical resistivity and specific heat measurements were carried out on Quantum Design Physical Property Measurement System (PPMS) equipped with dilution refrigerator assembly. The resistivity measurements were studied by the standard ac four-probe method, and specific heat by means of relaxation method in the temperature range down to 50 mK.

The crystal orbital Hamilton population (COHP) were calculated by means of tight-binding, linear muffin-tin orbital-atomic sphere approximation (TB-LMTO-ASA) program using Stuttgart code [17–20]. The space was filled with overlapping Wigner-Seitz (WS) spheres in the ASA method. The empty spheres were required to 100% fill up the space, and the overlapping in WS spheres was no greater than 16%. The WS radii are 4.034 Å for Sr, 2.889 Å for Pd, and 2.378 Å for P in $SrPd_2P_2$, and 3.915 Å for Ca, 2.895 Å for Pd, and 2.311 Å for P in $CaPd_2P_2$. The convergence criterion was set as 0.05 meV [20].

Electronic structure calculations were performed with a highly accurate all-electron full potential linearized augmented plane-wave (FP-LAPW) method [21] as implemented in the ELK code [22,23]. The exchange and correlation effects were treated using generalized gradient approximation (GGA) in the form proposed by Perdew, Wang, and Ernzerhof [24]. Spin-orbit coupling (SOC) was included as a second variational step, using scalar-relativistic eigenfunctions as the basis, after the initial calculation converged to self-consistency. The Monkhorst-Pack special k-point scheme [25] with the mesh $17 \times 17 \times 14$ was used in the first Brillouin zone sampling, and the value of RKmax parameter was set to 8. For the Fermi surfaces, the irreducible Brillouin zone was sampled by 8042 k points to ensure accurate determination of the Fermi level [26].

In order to calculate the vibrational properties of $CaPd_2P_2$ and $SrPd_2P_2$, we used the plane-wave pseudopotential method, through the QUANTUN ESPRESSO package [27,28]. The electron-ion interaction was described by using the scalar-relativistic optimized norm-conserving Vanderbilt (ONCV) pseudopotentials [29,30]. The calculations for both compounds were made with the kinetic energy cutoff of 70 Ry, using the same type of the exchange-correlation potential as in the ELK code. The Brillouin zones (BZs) were sampled by using the Monkhorst-Pack scheme with $8 \times 8 \times 8$ zone-centered grid for structure optimization and vibration properties. The electronic structure for experimental lattice parameters was checked thoroughly against the FP-APW+lo method and was found to be practically identical [31]. Since phonon calculations at the experimental lattice constants are likely to result in softer frequencies, and in consequence lower the predicted T_c than those calculated for relaxed atomic positions, relaxed structures for both compounds were determined within the pseudopotential code [32]. The phonon dynamic matrices were computed on a $4 \times 4 \times 4$ q-point mesh, and a Fourier interpolation was made to obtain phonon frequencies for any chosen q point. The Brillouin zone integration for the electron-phonon coupling within Migdal-Eliashberg theory [33–35] was done by using the $24 \times 24 \times 24$ k mesh with Gaussian smearing.

III. RESULTS AND DISCUSSION

Single-crystal x-ray diffraction refinement confirms that both compounds crystallize in a tetragonal $I4/mmm$ space group. The refinement results including atomic positions, site occupancies, and thermal displacements are summarized in Tables S1−S3 [36]. The PXRD patterns for $CaPd_2P_2$ and $SrPd_2P_2$ refined using Le Bail method are shown in Figs. 1(a) and 1(b), respectively. The red points and black solid lines represent experimental and calculated intensities, respectively. The analysis confirms that $CaPd_2P_2$ and $SrPd_2P_2$ crystallize in a tetragonal unit cell with the space group $I4/mmm$ (No. 139). All Bragg positions can be indexed in $I4/mmm$ space group and elemental Bi (marked as green [Fig. 1(a)] and pink [Fig. 1(b)] vertical lines, respectively). The obtained lattice parameters are $a = b = 4.1378(9)$ Å and $c = 9.6417(6)$ Å for $CaPd_2P_2$ ($\chi^2 = 1.14$), and $a = b = 4.2338(4)$ Å and $c = 9.6909(2)$ Å for $SrPd_2P_2$ ($\chi^2 = 1.07$), which are in good agreement with previous report [37].

The crystal structure of $CaPd_2P_2$ is shown in Fig. 1(e). Both $CaPd_2P_2$ and $SrPd_2P_2$ crystallize in a tetragonal $I4/mmm$ space group, and can be understood as the variant of layered $ThCr_2Si_2$-type structure. For comparison, we also show the structure of $BaFe_2As_2$ in Figs. 1(c) and 1(d), which exhibit the same tetragonal crystal structure. The iron arsenide layer $[Fe_2As_2]^{2-}$ is separated by Ba^{2+} ions, and the $[As−As]$ unit is equivalent to $[P−P]$ unit in $(Ca,Sr)Pd_2P_2$. The unit cell of $CaPd_2P_2$ and $SrPd_2P_2$ can be considered as $[Pd_2P_2]^{2-}$ layer [Fig. 1(f)] separated by alkali-earth metal cations (Ca^{2+}/Sr^{2+}). The two polyanionic $[Pd_2P_2]^{2-}$ layers form a cage for Ca^{2+}/Sr^{2+} ions, with the distances $d(Ca\text{-}P) = 3.1178(7)$ Å, $d(Ca\text{-}Pd) = 3.1776(2)$ Å, $d(Sr\text{-}P) = 3.1968(7)$ Å, and $d(Sr\text{-}Pd) = 3.2233(4)$ Å. The Pd-Pd and Pd-P distances within the layer for $CaPd_2P_2$ are 2.9252(3) and 2.4610(9) Å, respectively, and 2.9991(5) and 2.4982(1) Å, respectively, for $SrPd_2P_2$. The shorter Pd-P intralayer distance indicates stronger interaction compared to Pd-Pd, which can play a crucial role in stabilizing the crystal structure.

The temperature dependence of the electrical resistivity (ρ) measured between 50 mK and 300 K under zero applied magnetic field is presented in Figs. 2(a) and 2(b) for $CaPd_2P_2$ and $SrPd_2P_2$, respectively. The metallic behavior ($d\rho/dT > 0$) is observed for both compounds in the whole temperature range. Above 2 K, the $\rho(T)$ curves can be described by conventional Bloch-Grüneisen formula:

$$\rho(T) = \rho_0 + \rho_{BG} = \rho_0 + 4B_{el\text{-}ph}\Theta_D\left(\frac{T}{\Theta_D}\right)^5$$

$$\times \int_0^{\frac{T}{\Theta_D}} \frac{x^5 dx}{(e^x - 1)(1 - e^{-x})}, \quad (1)$$

where ρ_0 is the residual resistivity due to scattering of conduction electrons on lattice impurities, Θ_D is the Debye temperature, and $B_{el\text{-}ph}$ is a coefficient representing scattering strength of electrons with acoustic phonons. The estimated values obtained from the fits are $\rho_0 = 23.48(3)\,\mu\Omega\,cm$, $B_{el\text{-}ph} = 0.24(1)\,\mu\Omega\,cm\,K^{-1}$, and $\Theta_D = 232(1)\,K$ for $CaPd_2P_2$, and $\rho_0 = 67.79(4)\,\mu\Omega\,cm$, $B_{el\text{-}ph} = 0.39(1)\,\mu\Omega\,cm\,K^{-1}$, and $\Theta_D = 185(1)\,K$ for $SrPd_2P_2$ (see
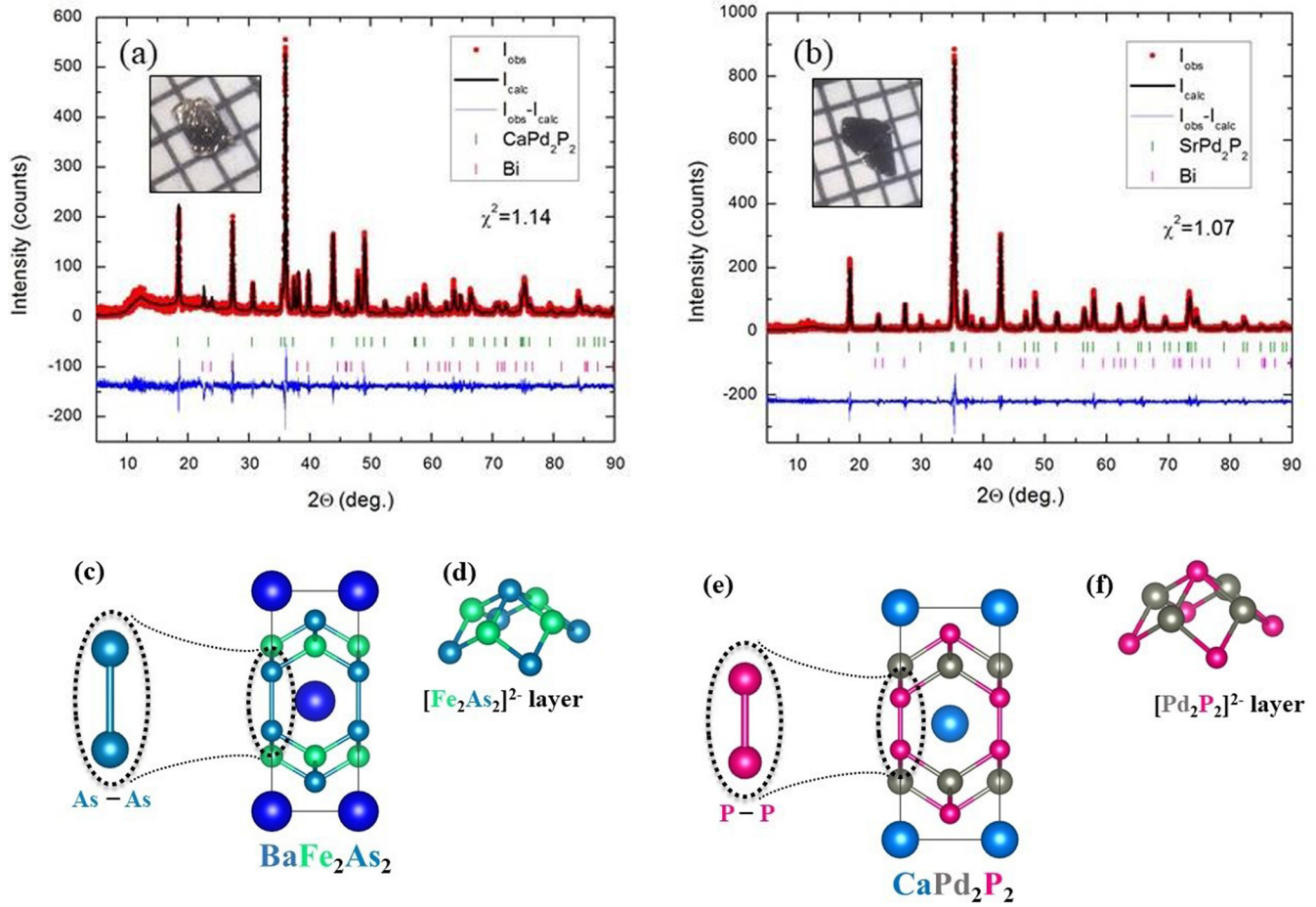
FIG. 1. Powder diffraction pattern of (a) $CaPd_2P_2$ and (b) $SrPd_2P_2$. The red points, black solid line, and blue solid line represent experimental data (I_{obs}), the calculated LeBail refinement (I_{calc}) and the difference between calculated and observed intensities ($I_{obs} - I_{calc}$), respectively. The vertical bars mark the expected Bragg positions. (Inset) The picture of obtained single crystals of (a) $CaPd_2P_2$ and (b) $SrPd_2P_2$. The crystal structure relation between $BaFe_2As_2$ and $CaPd_2P_2$. Crystal structure along crystallographic a axis for $BaFe_2As_2$ (c), and $CaPd_2P_2$ (e) with marked using a dashed line [As−As] (c) and [P−P] (e) units. The single layer of $[Fe_2As_2]^{2-}$ (d) and $[Pd_2B_2]^{2-}$ (f). The crystal structure data for $BaFe_2As_2$ come from reference [38].

Table I). The residual resistivity ratio RRR = $\rho(300\,K)/\rho(2\,K)$ is equal to 4 and 2.6 for $CaPd_2P_2$ and $SrPd_2P_2$, respectively. All obtained values are similar with previous report for $CaPd_2As_2$ and $SrPd_2As_2$ [39]. Below

TABLE I. Normal and superconductivity parameters of $CaPd_2P_2$ and $SrPd_2P_2$.

Parameter	Units	$CaPd_2P_2$	$SrPd_2P_2$
ρ_0	$\mu\Omega$ cm	23.48(3)	67.79(4)
$B_{el\text{-}ph}$	$\mu\Omega$ cm K^{-1}	0.24(1)	0.39(1)
$\Theta_D[\rho(T)]$	K	232(1)	185(1)
γ	mJ mol^{-1} K^{-2}	6.2(2)	6.13(2)
$\Theta_D[Cp]$	K	278(1)	302(1)
T_c	K	1.0	0.7
$\Delta C/\gamma T_c$	–	1.40	1.42
$\lambda_{el\text{-}ph}$	–	0.46	0.42
$N(E_F)$	States eV^{-1} f.u.$^{-1}$	1.74	1.77
$H_{c2}(0)$	Oe	935	625
ξ_{GL}	nm	592	724

2 K, the resistivity quickly drops to zero, suggesting the superconducting transition in both compounds.

To confirm the superconducting transition, the resistivity was further measured under the application of magnetic field. Figures 2(c) and 2(d) present $\rho(T)$ measured at indicated magnetic fields down to 50 mK for $CaPd_2P_2$ and $SrPd_2P_2$, respectively. Note that, for $CaPd_2P_2$, $\rho(T)$ starts to drop below 1.7 K accompanied with a much sharper drop below $\sim$1.0 K. The higher-temperature drop is gradually suppressed upon the application of magnetic field. We recall that α-PdBi$_2$ undergoes superconducting transition at 1.7 K [40,41]. Even it was not detected by powder x-ray diffraction, the small amount of α-PdBi$_2$ may be responsible for the anomaly at 1.7 K. Above 500 Oe, only one transition remains, which corresponds to the superconducting transition of $CaPd_2P_2$. At zero field, $T_c \sim 1.0$ K. For $SrPd_2P_2$, the resistivity drops to zero at $T_c \sim 0.7$ K. Upon the application of magnetic field, the transition temperature T_c is pushed to lower temperatures, consistent with the superconducting transition.

The upper critical field (H_{c2}) versus temperature for $CaPd_2P_2$ and $SrPd_2P_2$ is presented in Figs. 2(e) and 2(f), respectively. The superconducting temperature [$T_c(H)$],
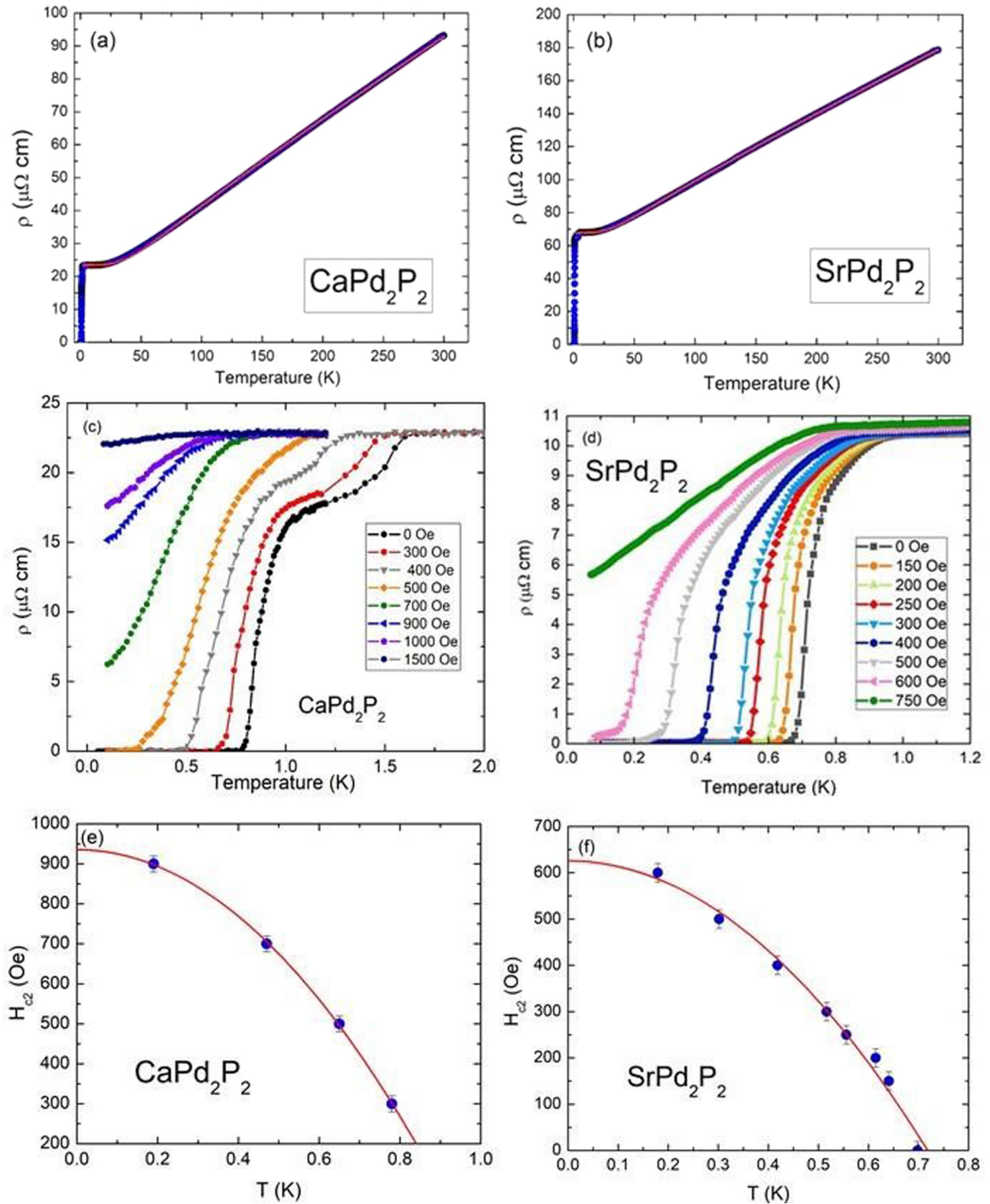
FIG. 2. The temperature dependence of resistivity measured under zero magnetic field for (a) $CaPd_2P_2$ and (b) $SrPd_2P_2$. The red solid line represents the fit discussed in the text. The low-temperature dependence of electrical resistivity measured under transverse applied magnetic field for (c) $CaPd_2P_2$ and (d) $SrPd_2P_2$. The upper critical field (H_{c2}) vs temperature for (e) $CaPd_2P_2$ and (f) $SrPd_2P_2$. The red solid line represent fit discussed in the text.

defined as the temperature at which the resistivity dropped by 50% from the normal state, was estimated for each applied magnetic field. The data were fitted using the BCS formula:

$$H_{c2}(T) = H_{c2}(0)\left[1 - \left(\frac{T}{T_c}\right)^2\right]. \qquad (2)$$

The obtained parameters are $H_{c2}(0) = 935$ Oe, $T_c = 0.95$ K for $CaPd_2P_2$, and $H_{c2}(0) = 625$ Oe, $T_c = 0.71$ K for $SrPd_2P_2$. From the Ginzburg-Landau formula:

$$\xi_{GL} = \sqrt{\frac{\Phi_0}{2\pi H_{c2}(0)}}, \qquad (3)$$

where $\Phi_0 = h/2e$ is the quantum magnetic flux, one can estimate the Ginzburg-Landau coherence length $\xi_{GL} = 592$ and 724 nm for $CaPd_2P_2$ and $SrPd_2P_2$, respectively.

To prove that observed superconductivity is the bulk property of $CaPd_2P_2$ and $SrPd_2P_2$, specific heat measurements are carried out for both compounds. The temperature dependence of the specific heat in the range of $0.5-300$ K is presented in Figs. 3(a) and 3(b) for $CaPd_2P_2$ and $SrPd_2P_2$, respectively. Note that, at high temperatures, C reaches the value expected for Dulong-Petit law: $3nR = 124.65$ J mol^{-1} K^{-1}, where R is the gas constant and n is the number of atoms per formula unit ($n = 5$ for APd_2P_2). To identify the anomaly associated with superconductivity, low-temperature specific heat is plotted in Fig. 3(c) and 3(d) as C/T versus T for $CaPd_2P_2$ and $SrPd_2P_2$, respectively. For each compound, there is a λ-shape jump, indicating a true phase transition. An equal-area construction [see the red solid lines in Figs. 3(c) and 3(d)] is done to determine the critical temperatures: $T_c = 1.0$ and 0.7 K for $CaPd_2P_2$ and $SrPd_2P_2$, respectively. This is consistent with T_c values obtained from the electrical resistivity.

According to the BCS theory, the specific heat jump ($\Delta C/\gamma T_c$) is expected to be 1.43 in the weak-coupling limit. Here, γ is the electronic specific heat in the normal state, which can be estimated from low-temperature specific heat above T_c. Figures 3(e) and 3(f) show C/T versus T^2 for $CaPd_2P_2$ and $Sr_2Pd_2P_2$, respectively. The data can be fitted using $C/T = \gamma + \beta T^2$, where the second term describes the lattice contribution to the specific heat with β related to the Debye temperature by the formula:

$$\Theta_D = \sqrt[3]{\frac{12\pi^4 nR}{5\beta}} \qquad (4)$$

The parameters obtained from the fits are $\gamma = 6.2(2)$ mJ mol^{-1} K^{-2}, $\Theta_D = 278(1)$ K for $CaPd_2P_2$ and $\gamma = 6.13(2)$ mJ mol^{-1} K^{-2}, $\Theta_D = 302(1)$ K for $SrPd_2P_2$. Thus $\Delta C/\gamma T_c$ is ~ 1.42 for $CaPd_2P_2$ and 1.47 for $SrPd_2P_2$. The significant discrepancy between Debye temperatures obtained from specific heat and electrical resistivity data may be caused by different contribution of phonon branches to thermodynamic and transport phenomena. Similar behavior was observed in other superconductors, such as $ScGa_3$ and YPd_2Si_2 [42,43].

Using the obtained (Θ_D) values from low-temperature capacity, and critical temperatures, the electron-phonon coupling constant (λ_{el-ph}) can be calculated using the inverted McMillan formula [44]:

$$\lambda_{el-ph} = \frac{1.04 + \mu^* \ln\left(\frac{\Theta_D}{1.45T_c}\right)}{(1 - 0.62\mu^*)\ln\left(\frac{\Theta_D}{1.45T_c}\right) - 1.04}. \qquad (5)$$

The Coulomb repulsion constant μ^* (which represents the strength of the screened Coulomb repulsion between the electrons in a Cooper pair) is considered as 0.13, the value of λ_{el-ph} was estimated at 0.46 and 0.42 for $CaPd_2P_2$ and $SrPd_2P_2$, respectively. This suggests that electron-phonon coupling is stronger in former than latter. In addition, the density of states (DOS) at the Fermi energy level [$N(E_F)$] can be calculated using the formula:

$$N(E_F) = \frac{3\gamma}{\pi^2 k_B^2(1 + \lambda_{el-ph})}, \qquad (6)$$

where k_B is the Boltzmann constant. The obtained value of $N(E_F)$ is 1.74 states/eV/f.u. and 1.77 states/eV/f.u. for $CaPd_2P_2$ and $SrPd_2P_2$, respectively. These values are slightly smaller than that reported previously [39].

For better understanding the relationship between chemical bonding and physical properties of $CaPd_2P_2$ and $SrPd_2P_2$, we calculated DOS and crystal orbital Hamilton population (-COHP). Figures 5(a) and 5(b) represent the obtained DOS and $-$COHP curves for $CaPd_2P_2$ and Figure 4(c) and 4(d) for $SrPd_2P_2$. For both compounds, Pd overlaps with P states near the Fermi energy, making main contribution to DOS. Pd-P and Pd-Pd bonding interactions are dominating below -3 eV in $-$COHP curves, which indicates strong hybridization between Pd and P orbits are important for stabilizing the phase. Above -3 eV, the atomic interactions are dominated by Pd-Pd and Pd-P antibonding, while alkali-earth metals form the bonding interactions with Pd and P. Around Fermi levels, the Pd-P and Pd-Pd interactions are primary. The strong antibonding interactions related to the electronic instability likely lead to structural distortion, magnetic ordering, even charge density waves (CDWs). The influence of antibonding interaction for superconducting properties were previously reported for several intermetallic compounds such as SrSnP, $BaPt_2Bi_2$, or NbRuB [9,45,46]. For (Ca,Sr)Pd_2P_2, the antibonding interaction may impact superconductivity as well.

The calculated values of the density of states at the Fermi energy $N(E_F)$ with SOC are 1.85 and 1.89 states/eV/f.u, which are in very good accordance with the experimental values of 1.74 and 1.77 states/eV/f.u. for $CaPd_2P_2$ and $SrPd_2P_2$, respectively.

The electronic band dispersion without and with SOC along various symmetry directions in the Brillouin zone of body centered tetragonal lattice for $CaPd_2P_2$ and $SrPd_2P_2$ are shown in Figs. 5(a) and 5(b), respectively. Both compounds have a metallic character with two highly dispersive bands crossing the Fermi level along the Γ_3-Z, Γ-Z, Γ-Γ_1, and Γ_1-Γ_2 symmetry directions. Between Γ-X-P-Γ_3 and Γ-Γ_2, valence and conduction bands are well separated from each other. As expected, overall both dispersion curves are very similar. However, some small differences due to the energy shift and distinctions in lattice parameters can be noticed, for example, near high symmetry points. In order to check how the inclusion of SOC influences the electronic structure, further self-consistent calculations were done with a term
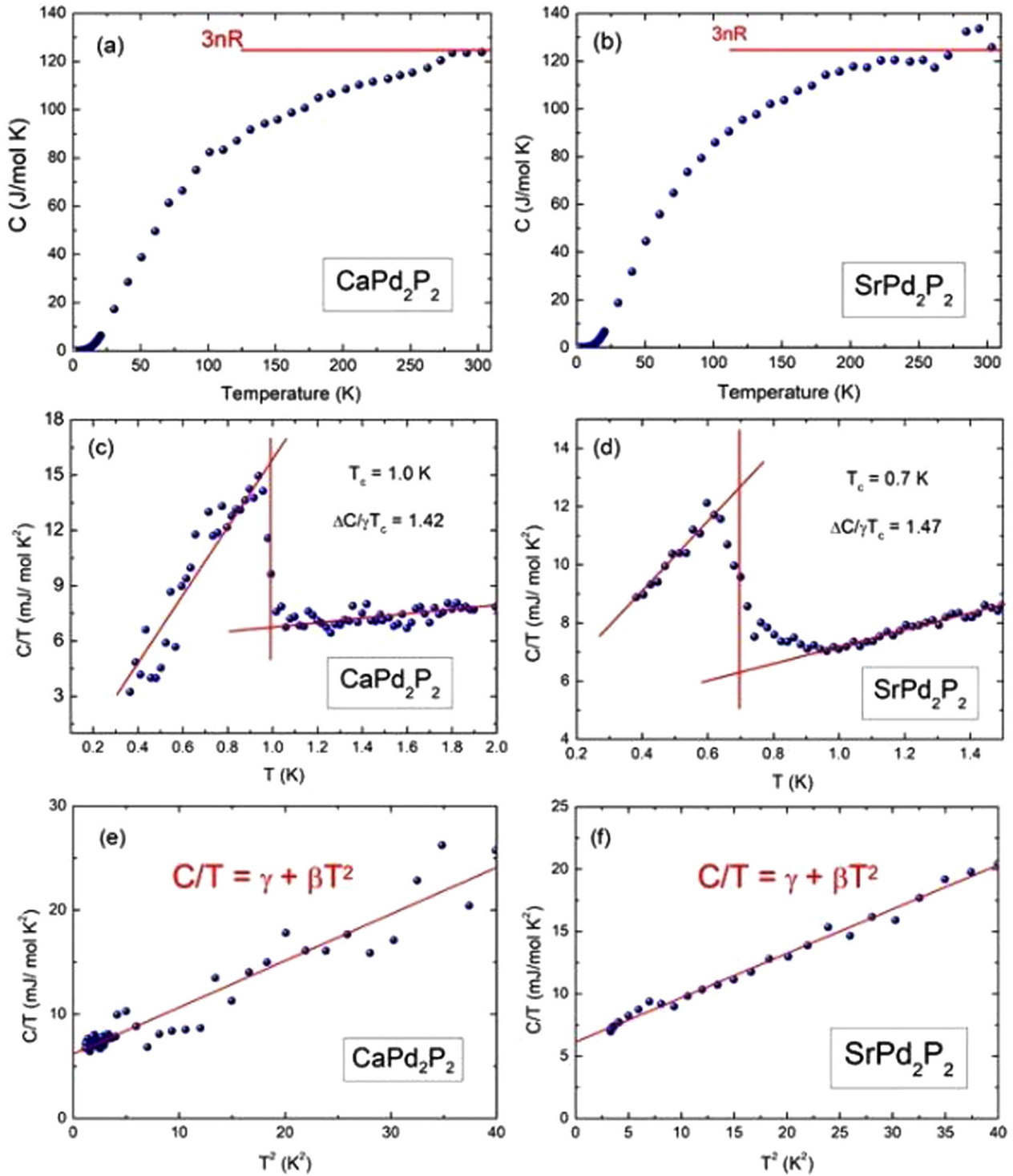
FIG. 3. The specific heat versus temperature measured in the range from 0.5 to 300 K for (a) $CaPd_2P_2$ and (b) $SrPd_2P_2$. The temperature dependence of C/T measured at zero applied magnetic field for (c) $CaPd_2P_2$ and (d) $SrPd_2P_2$. The solid red lines outline an equal-area entropy construction. The low-temperature range data plotted as C/T vs T^2 for (e) $CaPd_2P_2$ and (f) $SrPd_2P_2$. The red solid line represent fit discussed in the text.

$\sigma \cdot L$ added to the second-variational Hamiltonian. As can be regarded from Figs. 6(a) and 6(b), the effect of introducing SOC is very small, marginally lifting degeneracy in the band structure (for example, along Γ-Z direction), and not radically changings near Fermi level are observed in both compounds. Far from E_F most of the bands are also nearly unchanged

except a few gaps increase owing to a reduction of symmetry [47].

In both compounds, the calculations show that two bands cross the Fermi level, leading to nearly indistinguishable Fermi surface sheets, shown in Figs. 5(c) and 5(d). The first sheet has a truncated disklike shape centered at the Z point,
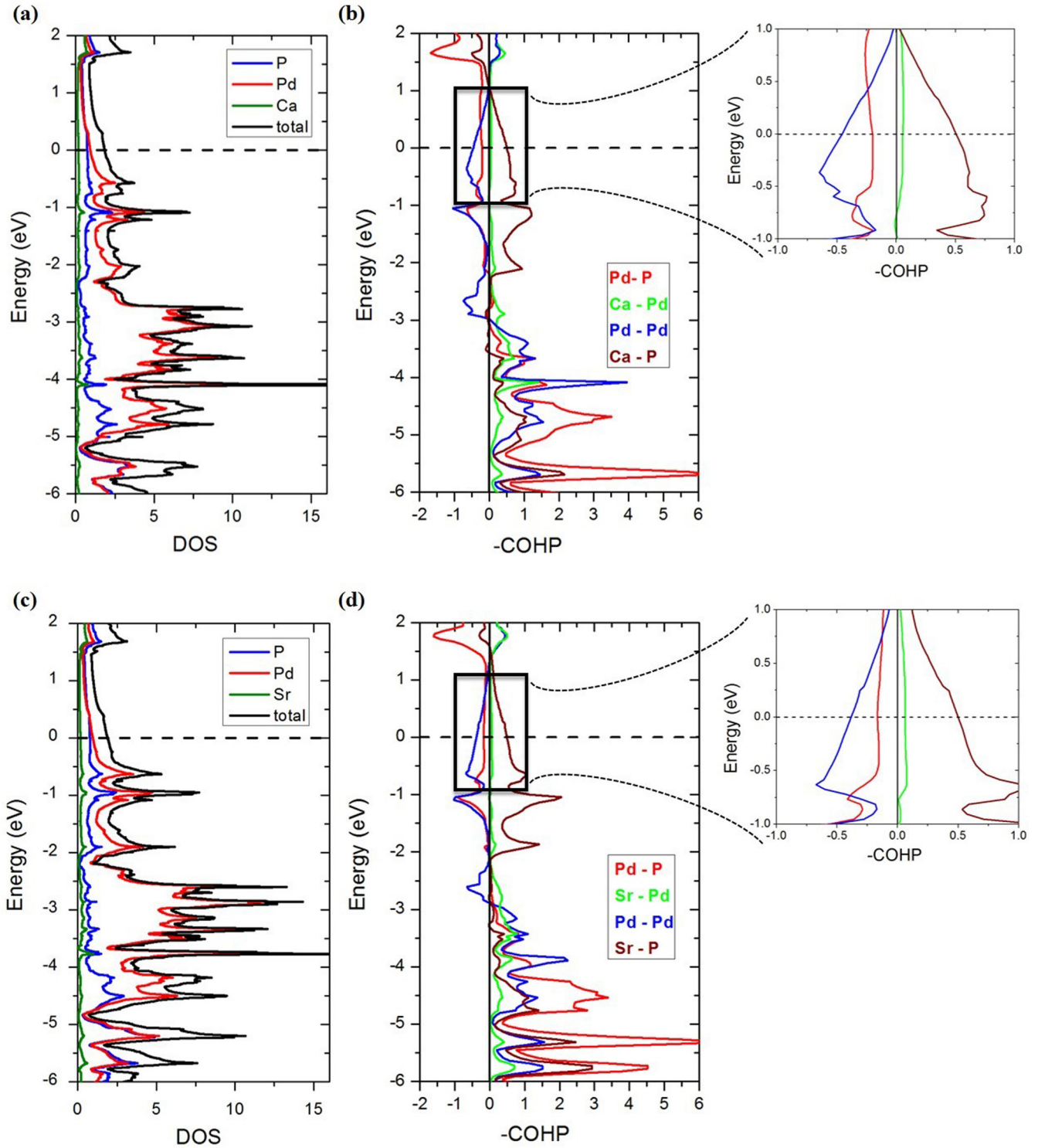
FIG. 4. Crystal orbital Hamilton population ($-$COHP) for $CaPd_2P_2$ (a) and $SrPd_2P_2$ (c) and calculated total and partial DOS of $CaPd_2P_2$ (b) and $SrPd_2P_2$ (d). The Fermi energy level is represented by a dashed line.

with additional four arms touching the edges of the Brillouin zone. The second sheet consists of a quasi-two-dimensional warped cylinder centered at the G point with four widen arms along X direction. These two FS shape largely resemble topology of other $ThCr_2Si_2$-type superconductors such as $LaPd_2As_2$ [48], $CaPd_2As_2$, and $SrPd_2As_2$ [49].

In general, according to the McMillan-Hopfield parameters for the superconductivity, the electron-phonon coupling constant may be expressed by [44,50,51]

$$\lambda_{el-ph} = \frac{N(E_F)\langle I^2 \rangle}{M \langle \omega^2 \rangle} \tag{7}$$
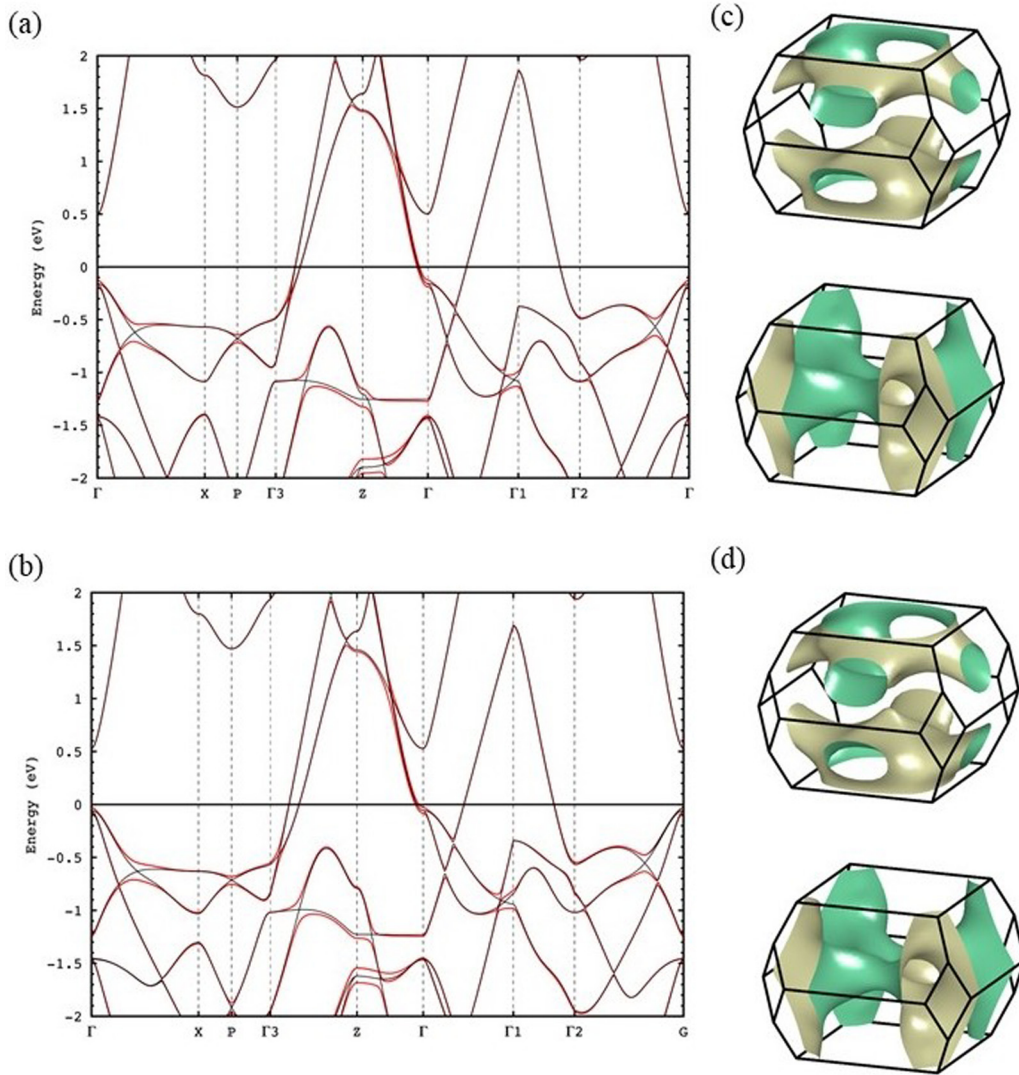
FIG. 5. Calculated electronic band structure along selected high symmetry directions in the bcc Brillouin [(a) and (b)] with (red lines) and without spin-orbit coupling. Corresponding Fermi surface sheets [(c) and (d)] of $CaPd_2As_2$ and $SrPd_2P_2$ with spin-orbit coupling.

where M is the atomic mass, $\langle \omega^2 \rangle$ is the average of squared phonon frequencies, which can be also approximated as $\langle \omega^2 \rangle = 0.5\Theta_D^2$, and $\langle I^2 \rangle$ is the Fermi surface average of squared electron-phonon coupling interaction. Along with the above equation, the value of electron-phonon coupling constant λ_{el-ph} decreases rapidly with increasing phonon frequency and the mass of the atoms. Since calculated and experimental values of $N(E_F)$ for both compounds are comparable, and assuming that (i) Pd and P phonon oscillations are particularly important for superconductivity in considered phases and (ii) both compounds have Fermi surfaces with similar topology, one can assume that slightly different values of Debye temperatures determine slightly inequality between λ_{el-ph} of 0.47 and 0.44 for $CaPd_2P_2$ and $SrPd_2P_2$, respectively.

The phonon energy dispersion curves along the high-symmetry directions of the Brillouin zone with the optimized crystal structure, together with the calculated total density of states as a function of energy, are presented in Fig. 6. We do not find any imaginary phonon frequency in the whole tetragonal Brillouin zone for both compounds. This feature

supports the dynamical stability of $CaPd_2P_2$ and $SrPd_2P_2$ in this structure type.

The overall both phonon spectrums can be divided into four separate energy regions. The low-frequency region ranges from 0 to 4.1 THz ($CaPd_2P_2$) and to 4.5 THz ($SrPd_2P_2$), the second to 6.0 THZ ($CaPd_2P_2$) and 6.3 THZ ($SrPd_2P_2$), whereas third middle frequency region falls in the range from 6.0 to 8.6 THz ($CaPd_2P_2$) and 6.3 to 8.9 THz ($SrPd_2P_2$). Finally, the highest maxima in the phonon DOSs are in noticeably shifted in the fourth energy range, e.g., between 12.1–12.4 THz, and 9.9 to 11 Thz, for $CaPd_2P_2$ and $SrPd_2P_2$, respectively. In consequence, both full phonon spectrums are lengthened than those for $CaPd_2As_2$ (7.1 THz) and $SrPd_2As_2$ (6.6 THz); however, their whole energy spectra ranges are comparable to the energy ranges of the isostructural ternary phosphides BaM_2P_2 (M = Ni, Rh, and Ir) with the same structure type [52]. This expansion in the frequency range can be regarded as an effect of the substitution of heavier As atoms with the lighter P atoms and the comparatively smaller unit cell volume of the $(Ca,Sr)Pd_2P_2$ compounds.
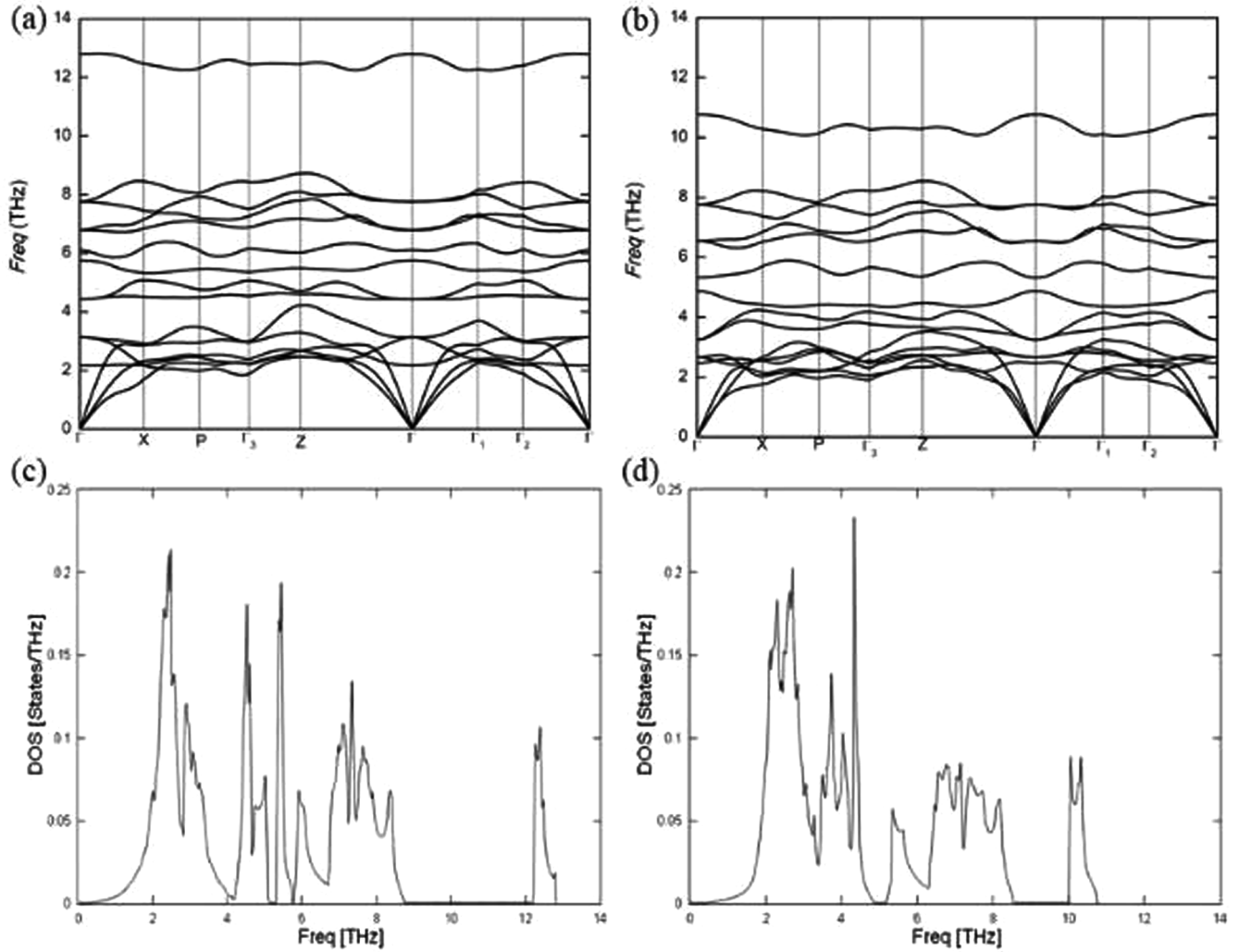
FIG. 6. Phonon dispersion curves [(a) and (b)] along high-symmetry directions in the Brillouin zone and density of states [(c) and (d)] at the optimized lattice parameters of $CaPd_2P_2$ and $SrPd_2As_2$.

In the first phonon energy region, the highest-frequency acoustic phonon branch disperses up to around 2.8 and 2.5 THz at two-third distance along Γ-Z direction for $CaPd_2P_2$ and $SrPd_2P_2$, respectively, where it nearly touches one of the low-frequency optical phonon branches. In $SrPd_2P_2$, the two lowest optical phonon branches are downshifted in this energy region, with the visible increase of their curvature. In a consequence, a gap along edges of the BZ completely disappears and there is significant overlap between the acoustic and optical branches.

In the second region, for both compounds, the two lower-frequency branches are degenerate at G point, whereas the other two are fully separated along all the directions in the BZ. In turn, in the third region, four branches are doubly degenerate only in the vicinity of the G point. These two fully separated bands in third region create a high peak in phonon DOS around 4.2 and 4.8 THz for $CaPd_2P_2$ and $SrPd_2P_2$, respectively. Close inspection of the atomic masses of Ca and Sr allows us to understand this difference between the two compounds, in the fully analogy to phonon band

dispersion for $CaPd_2As_2$ and $SrPd_2As_2$. Finally, both fourth highest regions include only one optical mode which slightly disperses. Like what was noticed in $SrPd_2As_2$ and $SrPd_2As_2$, here we can assume that the contributions to the highest frequency region are mostly due to contribution of lighter P atoms.

The calculated Eliashberg function $\alpha^2F(\omega)$ and average electron-phonon coupling constant $\lambda_{el\text{-}ph}$ are shown in Fig. 7. These yield electron-phonon coupling constants $\lambda_{el\text{-}ph}$ of 0.46 and 0.44 for $CaPd_2P_2$ and $SrPd_2P_2$, respectively, in ideal agreement with the presented experimental data.

In both compounds, the contributions of the first, third and fourth frequency regions contribute approximately 90% of the total $\lambda_{el\text{-}ph}$ for both compounds. Therefore the presented results of phonon calculations allow us to conclude, that Pd and P phonon branches are mostly dominated the superconductivity in $CaPd_2P_2$ and $SrPd_2P_2$. This result is fully expected by the electronic DOS calculations because Pd and P states dominate the electronic states close to the Fermi level.
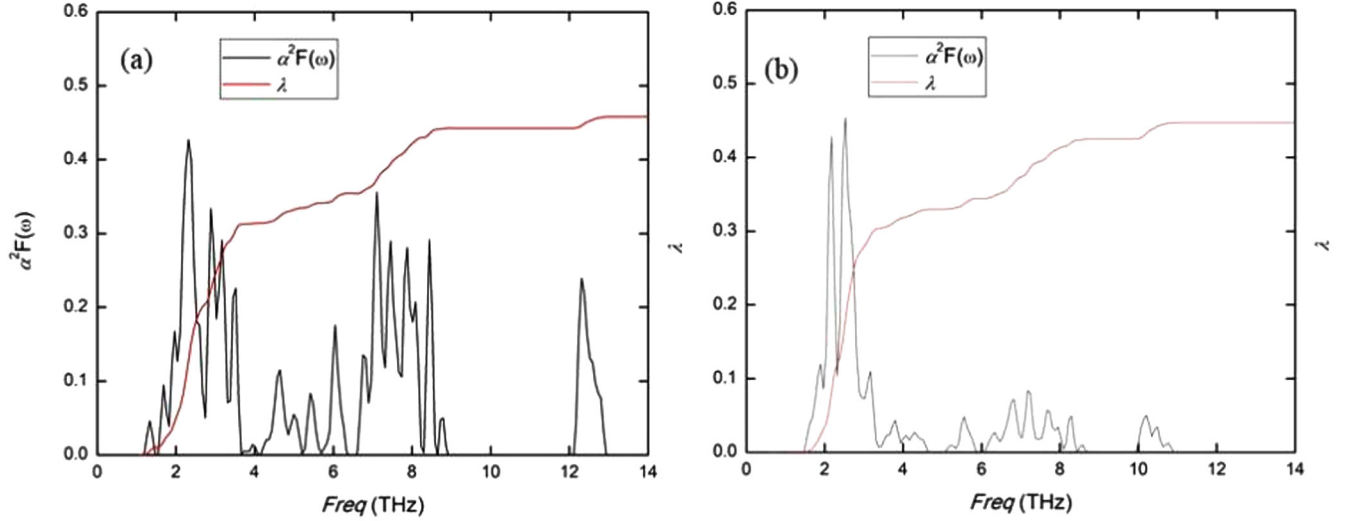
FIG. 7. Calculated isotropic Eliashberg spectral function $\alpha^2 F(\omega)$ (solid line) and integrated electron-phonon coupling strength λ (red line) of $CaPd_2As_2$ and $SrPd_2P_2$ superconductors at the optimized lattice parameters.

Finally, the superconducting critical temperature can be calculated using the Allen-Dynes formula [53]:

$$T_c = \frac{\omega_{\log}}{1.2} \exp\left[\frac{-1.04(1 + \lambda_{\text{el-ph}})}{\lambda_{\text{el-ph}}(1 - 0.62\mu^*) - \mu^*}\right], \qquad (8)$$

where the logarithmically averaged phonon frequency $\omega_{\log}$ takes the form

$$\omega_{\log} = \exp\left[\frac{2}{\lambda_{\text{el-ph}}} \int \frac{d\omega}{\omega} \alpha^2 F(\omega) \ln \omega\right] \qquad (9)$$

Using calculated $\lambda_{\text{el-ph}} = 0.46$ and $\omega_{\log} = 165.06\,\text{cm}^{-1}$ and choosing adjustable parameter $\mu^* = 0.12$ (values between 0.1 and 0.15 are considered as physically reasonable), a T_c of 0.96 K is obtained for $CaPd_2P_2$, which agrees remarkably well with the experimental value of 1.00 K. For $SrPd_2P_2$, $\lambda_{\text{el-ph}} = 0.4$ and $\omega_{\log} = 160.20\,\text{cm}^{-1}$, this gives a T_c of 0.72, which is again perfectly in accordance with the experimental value of 0.7 K.

IV. CONCLUSION

The new superconductors $CaPd_2P_2$ and $SrPd_2P_2$ have been successfully synthesized from the Bi-flux. The crystal structure and phase purity have been confirmed by XRD measurements. A combination of resistivity and heat capacity measurements unambiguously shows that $CaPd_2P_2$ and $SrPd_2P_2$ are bulk superconductors with $T_c \sim 1.0$ and 0.7 K, respec-

tively. The electronic and phonon structures were calculated by first-principles methods. The electronic structure analysis of $CaPd_2P_2$ and $SrPd_2P_2$ illustrates that the Pd-P antibonding interactions are key to the superconductivity. The work presented here indicates that the critical charge-transfer pairs can be a useful design paradigm for new superconductors.

[1] J. Bardeen, L. N. Cooper, and J. R. Schrieffer, Phys. Rev. **108**, 1175 (1957).

[2] J. G. Bednorz and K. A. Müller, Z. Phys. B: Condens. Matter **64**, 189 (1986).

[3] A. S. Sefat, R. Jin, M. A. McGuire, B. C. Sales, D. J. Singh, and D. Mandrus, Phys. Rev. Lett. **101**, 117004 (2008).

[4] M. Rotter, M. Tegel, and D. Johrendt, Phys. Rev. Lett. **101**, 107006 (2008).

[5] M. K. Wu, J. R. Ashburn, C. J. Torng, P. H. Hor, R. L. Meng, L. Gao, Z. J. Huang, Y. Q. Wang, and C. W. Chu, Phys. Rev. Lett. **58**, 908 (1987).

[6] K. Kudo, Y. Nishikubo, and M. Nohara, J. Phys. Soc. Jpn. **79**, 123710 (2010).

[7] B. Lv, B. I. Jawdat, Z. Wu, M. Sorolla, M. Gooch, K. Zhao, L. Deng, Y.-Y. Xue, B. Lorenz, A. M. Guloy, and C.-W. Chu, Inorg. Chem. **54**, 1049 (2015).

[8] C. Geibel, U. Ahlheim, C. D. Bredl, J. Diehl, A. Grauel, R. Helfrich, H. Kitazawa, R. Köhler, R. Modler, M. Lang, C. Schank, S. Thies, F. Steglich, N. Sato, and T. Komatsubara, Phys. C Supercond. **185–189**, 2651 (1991).

[9] X. Gui, L. Xing, X. Wang, G. Bian, R. Jin, and W. Xie, Inorg. Chem. **57**, 1698 (2018).

[10] N. Berry, C. Capan, G. Seyfarth, A. D. Bianchi, J. Ziller, and Z. Fisk, Phys. Rev. B **79**, 180502(R) (2009).

[11] T. Mine, H. Yanagi, T. Kamiya, Y. Kamihara, M. Hirano, and H. Hosono, Solid State Commun. **147**, 111 (2008).

[12] M. Sardar and D. Sa, Phys. C Supercond. Appl. **411**, 120 (2004).

[13] G. M. Sheldrick, Acta Crystallogr. Sect. C Struct. Chem. **71**, 3 (2015).

[14] H. M. Rietveld, J. Appl. Crystallogr. **2**, 65 (1969).

[15] J. Rodríguez-Carvajal, Phys. B: Condens. Matter **192**, 55 (1993).

[16] K. Momma and F. Izumi, J. Appl. Crystallogr. **44**, 1272 (2011).

[17] M. Elstner, D. Porezag, G. Jungnickel, J. Elsner, M. Haugk, Th. Frauenheim, S. Suhai, and G. Seifert, Phys. Rev. B **58**, 7260 (1998).

[18] O. K. Andersen and O. Jepsen, Phys. Rev. Lett. **53**, 2571 (1984).

[19] O. Jepsen and O. K. Andersen, The Stuttgart TB-LMTO-ASA Program 47, Germany (2000).

[20] R. Dronskowski and P. E. Bloechl, J. Phys. Chem. **97**, 8617 (1993).

[21] D. J. Singh and L. Nordstrom, *Planewaves, Pseudopotentials, and the LAPW Method* (Springer Science & Business Media, 2006).

[22] The ELK LAPW code, http://elk.sourceforge.net.

[23] G. P. Srivastava, J. Phys. Math. Gen. **17**, L317 (1984).

[24] J. P. Perdew, K. Burke, and M. Ernzerhof, Phys. Rev. Lett. **77**, 3865 (1996).

[25] H. J. Monkhorst and J. D. Pack, Phys. Rev. B **13**, 5188 (1976).

[26] A. Kokalj, Comput. Mater. Sci. **28**, 155 (2003).

[27] P. Giannozzi *et al.*, J. Phys.: Condens. Matter **21**, 395502 (2009).

[28] P. Giannozzi *et al.*, J. Phys.: Condens. Matter **29**, 465901 (2017).

[29] M. Schlipf and F. Gygi, Comput. Phys. Commun. **196**, 36 (2015).

[30] D. R. Hamann, Phys. Rev. B **88**, 085117 (2013).

[31] K. Lejaeghere *et al.*, Science **351**, aad3000 (2016).

[32] D. Billington, S. A. C. Nickau, T. Farley, J. R. Ward, R. F. Sperring, T. E. Millichamp, D. Ernsting, and S. B. Dugdale, J. Phys. Soc. Jpn. **83**, 044710 (2014).

[33] A. B. Migdal, Sov Phys. JETP **7**, 996 (1958).

[34] G. M. Eliashberg, Sov Phys. JETP **11**, 696 (1960).

[35] J. P. Carbotte, Rev. Mod. Phys. **62**, 1027 (1990).

[36] See Supplemental Material at http://link.aps.org/supplemental/10.1103/PhysRevMaterials.4.014801 for single-crystal x-ray diffraction refinement results.

[37] W. Jeitschko and W. K. Hofmann, J. Common Met. **95**, 317 (1983).

[38] R. Mittal, S. K. Mishra, S. L. Chaplot, S. V. Ovsyannikov, E. Greenberg, D. M. Trots, L. Dubrovinsky, Y. Su, Th. Brueckel, S. Matsuishi, H. Hosono, and G. Garbarino, Phys. Rev. B **83**, 054503 (2011).

[39] V. K. Anand, H. Kim, M. A. Tanatar, R. Prozorov, and D. C. Johnston, Phys. Rev. B **87**, 224510 (2013).

[40] K. Dimitri, M. M. Hosen, G. Dhakal, H. Choi, F. Kabir, C. Sims, D. Kaczorowski, T. Durakiewicz, J.-X. Zhu, and M. Neupane, Phys. Rev. B **97**, 144514 (2018).

[41] S. Mitra, K. Okawa, S. Kunniniyil Sudheesh, T. Sasagawa, J.-X. Zhu, and E. E. M. Chia, Phys. Rev. B **95**, 134519 (2017).

[42] E. Svanidze and E. Morosan, Phys. Rev. B **85**, 174514 (2012).

[43] G. Chajewski, P. Wiśniewski, D. Gnida, A. P. Pikul, and D. Kaczorowski, Cryst. Growth Des. **19**, 2557 (2019).

[44] W. L. McMillan, Phys. Rev. **167**, 331 (1968).

[45] W. Xie, H. Luo, K. Baroudi, J. W. Krizan, B. F. Phelan, and R. J. Cava, Chem. Mater. **27**, 1149 (2015).

[46] X. Gui, Z. Sobczak, T.-R. Chang, X. Xu, A. Huang, S. Jia, H.-T. Jeng, T. Klimczuk, and W. Xie, Chem. Mater. **30**, 6005 (2018).

[47] L. M. Schoop, F. Pielnhofer, and B. V. Lotsch, Chem. Mater. **30**, 3155 (2018).

[48] B. Singh and P. Kumar, AIP Conf. Proc. **1832**, 130061 (2017).

[49] I. R. Shein, S. L. Skornyakov, V. I. Anisimov, and A. L. Ivanovskii, J. Supercond. Nov. Magn. **27**, 155 (2014).

[50] J. J. Hopfield, Phys. Rev. **186**, 443 (1969).

[51] J. M. Ziman, *Electrons and Phonons: The Theory of Transport Phenomena in Solids* (OUP, Oxford, 2001).

[52] E. Karaca, H. M. Tütüncü, G. P. Srivastava, and S. Uğur, Phys. Rev. B **94**, 054507 (2016).

[53] P. B. Allen and R. C. Dynes, J. Phys. C: Solid State Phys. **8**, L158 (1975).